Title

Pulsed Laser Microbeam-Induced Cell Lysis: Time-Resolved Imaging and Analysis of Hydrodynamic Effects

Journal

Biophysical Journal, 91(1)

ISSN

0006-3495

Authors

Rau, Kaustubh R
Quinto-Su, Pedro A
Hellman, Amy N
et al.

Publication Date

2006-07-01

DOI

10.1529/biophysj.105.079921

Pulsed Laser Microbeam-Induced Cell Lysis: Time-Resolved Imaging and Analysis of Hydrodynamic Effects

Kaustubh R. Rau,*† Pedro A. Quinto-Su,*‡ Amy N. Hellman,*¶ and Vasan Venugopalan*†‡
*Laser Microbeam and Medical Program, Beckman Laser Institute, †Department of Biomedical Engineering, and ‡Department of Chemical Engineering and Materials Science, University of California, Irvine, California; and ¶Department of Bioengineering, University of California, San Diego, California

ABSTRACT Time-resolved imaging was used to examine the use of pulsed laser microbeam irradiation to produce cell lysis. Lysis was accomplished through the delivery of 6 ns, $\lambda = 532$ nm laser pulses via a $40\times$, 0.8 NA objective to a location 10 μm above confluent monolayers of PtK_2 cells. The process dynamics were examined at cell surface densities of 600 and 1000 cells/mm^2 and pulse energies corresponding to $0.7\times$, $1\times$, $2\times$, and $3\times$ the threshold for plasma formation. The cell lysis process was imaged at times of 0.5 ns to 50 μs after laser pulse delivery and revealed the processes of plasma formation, pressure wave propagation, and cavitation bubble dynamics. Cavitation bubble expansion was the primary agent of cell lysis with the zone of lysed cells fully established within 600 ns of laser pulse delivery. The spatial extent of cell lysis increased with pulse energy but decreased with cell surface density. Hydrodynamic analysis indicated that cells subject to transient shear stresses in excess of a critical value were lysed while cells exposed to lower shear stresses remained adherent and viable. This critical shear stress is independent of laser pulse energy and varied from ~60–85 kPa for cell monolayers cultured at a density of 600 cells/mm^2 to ~180–220 kPa for a surface density of 1000 cells/mm^2. The implications for single cell lysis and microsurgery are discussed.

INTRODUCTION

In the field of cell biology, pulsed laser radiation focused at high numerical apertures (i.e., pulsed laser microbeams) has been used to create damage on cellular and subcellular levels for over 40 years (1,2). More recently, laser microbeams have found an increasing number of applications in biotechnology (3,4). Lin and co-workers have demonstrated the use of 20-ns laser pulses at $\lambda = 532$ or 565 nm for selective killing of cells loaded with microparticles and nanoparticles within a mixed cell population (5,6). A commercial apparatus based on the use of pulsed laser microbeams for selective cell killing has also been described (7). Laser microdissection using UV laser pulses at $\lambda = 337$ nm is proving to be an important technique enabling the microanalysis of intracellular structures (8). In the area of single cell bioanalytics, the Allbritton group has developed the laser micropipette system for measurement of enzyme activity within single cells (9,10). In this technique, a Q-switched (Q-sw) Nd:YAG laser at $\lambda = 532$ nm is used to both lyse a single cell and mix the cellular contents with the surrounding medium. The cell contents are subsequently taken up by a glass capillary positioned above the cell, wherein they are electrophoretically separated and subsequently analyzed using laser-induced fluorescence. This technique shows great promise for analyzing the activity of biomolecules involved in signaling pathways with nanomolar sensitivity (11). A particular advantage is the fast timescale of the lysis process that rapidly stops all biochemical reactions by disrupting the cell and mixing its contents. The noncontact means of laser-based cell lysis is also attractive for integration with microfluidic chip-based devices (12).

Despite these innovative utilizations of laser microbeams in biology, there have been relatively few examinations of the basic mechanisms of laser-induced cell injury. A deeper understanding of laser-cell interactions is necessary for the continued development of laser microbeams as research tools as well as implementation for practical application. Laser-cell interaction mechanisms can be complex involving photothermal, photochemical, and photomechanical processes (13,14). The relative contributions of these processes in a given laser-cell interaction is governed by many factors including irradiation wavelength, pulse duration, pulse energy, and beam diameter. A number of researchers have demonstrated the utility of nanosecond pulses from the Q-switched (Q-sw) frequency-doubled Nd:YAG laser ($\lambda = 532$ nm) for cell lysis (9), microsurgery (15), and optoporation (16). Q-sw frequency-doubled Nd:YAG lasers are attractive for laser microbeam systems due to the visible laser radiation, low cost, small system footprint, and ease of operation. At this wavelength, there is little endogenous absorption by cellular components to provide deposition of laser energy. Even so, with the use of appropriate laser parameters, it is possible to precisely dissect cellular organelles or lyse single cells with minimal collateral damage.

Early in the application of laser microbeams in cell biology, Berns and co-workers noted that nonlinear optical processes such as multiphoton absorption and/or optical breakdown might be operative mechanisms for cell damage

Submitted December 19, 2005, and accepted for publication March 29, 2006.

P. A. Quinto-Su and A. N. Hellman contributed equally to this work.

Address reprint requests to Vasan Venugopalan, Tel.: 949-824-5802; E-mail: vvenugop@uci.edu.

K. R. Rau's present address is National Centre for Biological Sciences, Tata Institute of Fundamental Research, Bangalore 560 065, India.

0006-3495/06/07/317/13 $2.00 doi: 10.1529/biophysj.105.079921

(1,17,18). Recent work from our group (19,20) has demonstrated that the laser pulse energies and irradiances necessary to achieve optical breakdown in water using nanosecond pulses at $\lambda = 532$ or 1064 nm are similar to those used in nanosecond pulsed laser microbeam cell lysis and optoinjection (16), thereby implicating plasma formation as the initiating event for these processes.

Although studies regarding the interaction of laser-induced plasmas with cells are limited, an understanding of laser-induced plasma formation in tissue is well developed due to its now-widespread use in ophthalmic surgery (21). In such applications nanosecond laser pulses with a pulse energy of ~1 mJ or picosecond laser pulses of lower energy (80–300 μJ) are delivered at small focusing angles (8–30°) into an aqueous medium or within the bulk of a soft tissue, e.g., the corneal stroma, to cause controlled damage. The high irradiances achieved within the focal volume results in ionization even in the absence of endogenous absorption in the tissue. Downstream effects from the resulting plasma formation include shock wave propagation and cavitation bubble formation, expansion, and collapse, all of which can produce undesirable collateral damage (22). As a result, much attention has been given to understanding the relationship between the laser parameters (wavelength, pulse duration, energy, and focus angle) and the subsequent degree of tissue injury (23–25).

In general, studies examining the effects of laser pulses in tissue have utilized techniques such as histology and electron microscopy. These studies, while valuable, have provided little insight into the time evolution of the injury process. Juhasz and co-workers have examined the effects of picosecond and femtosecond laser pulses on bovine corneas in an ex vivo system (26,27). In these experiments, laser pulses were focused at depths of ~20 μm into the cornea. Using time-resolved imaging, the shock wave propagation and cavitation bubble dynamics were visualized and provided a means to estimate the shock pressures, maximum bubble diameter, and bubble collapse time in corneal tissue. However, the imaging system had insufficient spatial resolution to visualize the effects of the cavitation dynamics on the corneal epithelia or stroma. As a result, no firm conclusions could be drawn regarding the relationship between the mechanical effects and the observed tissue response.

Vogel and co-workers have examined the interaction of pulsed laser radiation with durations in the nanosecond-to-femtosecond range on ex vivo corneal tissue samples surrounded by aqueous media using a variety of techniques (23–25). In an early study, electron microscopy and histology were used to examine the effects produced by laser pulses that were focused proximal to the corneal epithelium in various irradiation geometries (23). This study revealed that the damage caused by laser pulses consisted of tissue puncture surrounded by a region denuded of cells. Both these effects were attributed to the cavitation bubble collapse and jet formation that follow laser-induced plasma formation. Subsequent studies also employed a time-resolved imaging system to study dynamic effects of laser-induced plasmas in corneal tissue (24,28). Time-resolved imaging of cavitation dynamics in the acellular stroma revealed that the high viscosity/stiffness of tissue reduced significantly the maximum bubble size as compared to cavitation in water. The bubble shape was also observed to be influenced by the spatial arrangement of collagen lamellae in the stroma. However, the action of laser pulses on corneal epithelium was not studied using the time-resolved imaging system. As a result, the specific events after laser-induced plasma formation responsible for the resulting cellular and tissue injury were not observed directly.

Whereas the studies by the groups of Juhasz and Vogel are quite valuable in orienting one to the potential damage mechanisms operative in laser-induced plasma formation within tissue, the parameters employed in the use of pulsed laser microbeams for targeted cell lysis, microsurgery, and transfection involve much lower pulse energies ($\lesssim$30 μJ) delivered via high numerical aperture objectives providing significantly larger focusing angles of 90–150°. Moreover, few studies have examined the temporal evolution of the damage processes initiated by pulsed laser microbeams with the use of high-resolution imaging techniques. Lin and co-workers have used time-resolved imaging to study the cavitation-induced damage produced in single cells containing either melanosomes or gold nanoparticles when irradiated by a 20-ns laser pulse from a frequency-doubled Nd:YAG laser (5,6). Absorption of the laser energy by melanosomes or gold nanoparticles produced heating and vaporization of the surrounding cytosol leading to bubble formation, expansion, and collapse. Although the bubble dynamics were implicated as the primary agent of the resulting cellular injury, they were not examined in detail and left unresolved the specific features of the process that were responsible for the cellular injury.

Our group recently reported the use of a time-resolved imaging system with ~1-μm spatial resolution and 0.5-ns temporal resolution to study laser-induced cell lysis in adherent cells (20). This system provided a detailed visualization of the cellular injury process, including plasma formation, shock wave propagation, and cavitation bubble formation, expansion, and collapse. These images revealed cavitation bubble expansion as the principal contributor to cell lysis and the maximum cavitation bubble size to be much larger than the zone of cell lysis. This was an important result, since it had long been thought that cavitation bubble collapse was the principal mechanism for mechanical damage produced by laser-induced plasma formation. The results also indicated that many of the cells that remain adherent after the lysis process remain viable, even though they were subject to severe transient deformation caused by the fluid motion associated with the cavitation dynamics.

Our earlier study provided the first exposition of the sequence of events produced by pulsed laser microbeam cell

lysis and identified cavitation bubble expansion as the primary agent of the damage process. However, these observations were not supported with substantial modeling or analysis to provide insight into potential relationships between the laser parameters and cavitation bubble characteristics to the spatial extent of cellular damage. To examine this issue in more detail, we have expanded significantly the range of our experimental study through the visualization and measurement of both the dynamics of the cell lysis process and the spatial extent of resulting cellular injury at four pulse energies corresponding to 0.7×, 1×, 2×, and 3× the threshold for plasma formation. These dynamics have been measured when focusing the laser pulses at high numerical apertures at a distance of 10-μm above fully confluent PtK_2 cell cultures with cell surface densities of 600 and 1000 cells/mm^2. Moreover, to complement this expanded set of data, we have developed a hydrodynamic model to predict the dynamic shear stresses experienced by adherent cells due to the displacement of fluid produced by the cavitation bubble expansion. The model predictions are data-driven. That is, the predictions are based on the time-resolved measurement of the cavitation bubble dynamics. This model provides, for the first time, estimates of the time-resolved shear stresses experienced by adherent cells as a function of both radial position and time after delivery of the laser pulse.

MATERIALS AND METHODS

Cell irradiation

An inverted microscope (Axiovert S100, Zeiss, Jena, Germany) was used as the experimental platform. A Q-sw, frequency-doubled Nd:YAG laser (INDI 20, Spectra Physics, Mountain View, CA) emitting 6 ns duration pulses at $\lambda = 532$ nm was used for cell irradiation. As shown in Fig. 1, the laser output was split into two beam lines using a $\lambda/2$ plate and polarization-sensitive beam splitter. The beam line formed by the reflection off the beam splitter was used for image illumination as described in Imaging System, below. The beam that passed through the beam splitter was expanded and recollimated using a 5× beam expander, followed by an iris to select the central portion of the laser beam. The beam emerging from the iris was introduced into the microscope epifluorescence port and reflected upward into the rear entrance aperture of the objective by a dichroic mirror placed in the microscope filter cube. The laser pulse energy was adjusted by rotating a linear polarizer inserted into the beam path. The laser pulse energy entering the rear entrance aperture of the objective was measured by removing the objective from the microscope turret and allowing the unobstructed beam to illuminate an energy detector (Model No. J3-05, Molectron, Santa Clara, CA) set on the microscope stage. Pulse-to-pulse energy variation was found to be ±3%. A bright-field objective (40×, 0.8 NA, Achroplan, Zeiss) was used for cell irradiation and visualization. Unless stated otherwise, the focal plane of the pulsed laser microbeam was positioned at a separation distance of $s = 10$ μm above the cell monolayer.

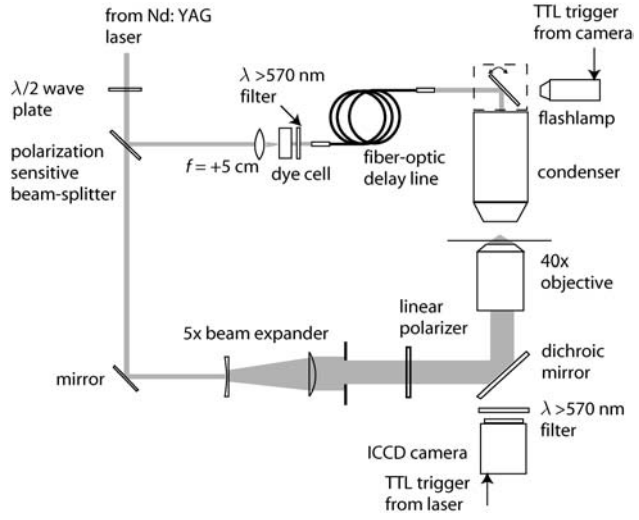

FIGURE 1 Schematic of laser-microscope setup for cell lysis and time-resolved imaging.

Imaging system

As depicted in Fig. 1, illumination for the time-resolved images was provided by delivering a short light pulse at the desired time delay after the arrival of the Nd:YAG laser pulse at the sample. At time delays shorter than 1.2 μs, illumination was provided by the fluorescence emission of a dye cell that was pumped by the beam line formed by the portion of the Nd:YAG laser beam that is reflected by the polarization-sensitive beam splitter. The dye fluorescence (Model No. LDS 698, Exciton, Dayton, OH) was coupled into a 600-μm-diameter multimode optical fiber (Model No. UMT 600, Thor Labs, Newton, NJ) with the fiber output being directed into the microscope condenser. Optical fibers of different length were used to provide the desired time delay between delivery of the pulsed laser microbeam to the target and the image illumination. The fluorescence emission from the dye cell provided illumination at $\lambda = 698 \pm 20$ nm with full width at half-maximum duration of 15 ns. The broad spectral width of the fluorescence emission provided images free from speckle artifact. At longer time delays, illumination was provided by an ultrashort duration flash lamp (Nanolite KL-L, High-Speed Photo System, Wedel, Germany) that was electronically triggered from the camera. The flash lamp emission provided a broad spectral output ($\lambda = 400$–700 nm) with a full width at half-maximum duration of 40 ns.

Images were acquired using a gated intensified CCD camera (PI-MAX, Roper Scientific, Trenton, NJ) that was triggered by a TTL pulse from the laser Q-switch. The camera operation and image acquisition was performed using WinView imaging software (Princeton Instruments, Trenton, NJ). The camera gate duration was set to 0.5 ns when using the fluorescent dye cell for illumination and to 200 ns when using flash lamp illumination due to electronic jitter in the flash lamp triggering. Thus, for time delays shorter than 1.2 μs, the exposure duration was governed by the 0.5-ns camera gate width, while at longer time delays the exposure duration was governed by the 40-ns duration of the flash lamp. A longpass filter (Model No. LP 570, Edmund Optics, Barrington, NJ) was used to prevent scattered laser radiation from reaching the camera. This system allowed us to irradiate and image the sample at the time delays of 0.5 ns to 50 μs required to capture the full dynamics of the process.

Cell culture

Potorous rat kidney epithelial (PtK_2) cells were grown in polystyrene culture dishes with glass bottoms (P35G-1.5-7-C, MatTek, Ashland, MA) in minimum essential medium (MEM, Gibco, Carlsbad, CA) supplemented with 10% fetal calf serum, L-glutamine, essential amino acids, sodium pyruvate, penicillin, and streptomycin. The culture medium was prepared free of phenol red to ensure its transparency to $\lambda = 532$ nm radiation. Culture dishes with cells at 100% confluency were used in each experiment. These

cells did not exhibit contact inhibition and thus the surface density of cells (cells/mm^2) was measured and controlled. The results below are provided for cell monolayers cultured at surface densities of 600 and 1000 cells/mm^2. Cell surface densities were determined by counting the number of cells in a square 0.5 mm $\times$ 0.5 mm region centered at the site of cell lysis. For a given cell surface density, the site-to-site variation was kept below 10%.

RESULTS

Plasma threshold measurement

Before conducting the cell lysis experiments, we determined the threshold for plasma formation in our experimental system. This was achieved by delivering an Nd:YAG laser pulse via the 40×, 0.8 NA bright-field objective into a petri dish filled with culture medium. Plasma formation in the culture medium was observed visually in a dark room and its incidence for 50 pulses at discrete pulse energies was recorded. The probability of plasma formation p as a function of pulse energy E_p was fit to a Gaussian error function given by

$$p(E_p) = 0.5\{1 + \mathrm{erf}[A_1(E_p + A_2)]\}, \quad (1)$$

where $\mathrm{erf}(x) \equiv 2/\sqrt{\pi}\int_0^x \exp(-\eta^2)d\eta$. The values A_1 and A_2 are the fitted parameters where A_1 governs the sharpness of the Gaussian error function and $|A_2|$ provides the threshold for plasma formation defined as the pulse energy that results in a 50% probability of plasma formation. Equation 1 describes accurately the stochastic nature of the plasma formation process (29). The result of one such experiment along with the model fit is shown in Fig. 2. Using the setup described in Materials and Methods resulted in a plasma threshold value of 8 $\pm$ 0.3 μJ. No difference in the plasma formation threshold was measured between culture medium and distilled water.

Earlier experiments by Venugopalan and co-workers that delivered 6-ns pulses from a Q-sw Nd:YAG laser via a 0.9 NA objective into an open cuvette filled with distilled water yielded a breakdown threshold of 1.9 μJ (19). These experiments were performed using an externally seeded laser whose output beam possessed a M^2 beam propagation factor of $\sim$1.4 (personal communication, Alfred Vogel, Institute of Biomedical Optics, University of Lübeck, Germany). This resulted in a threshold irradiance (I_{th}) of 7.8×10^{10} W/cm^2, when assuming a diffraction-limited spot size for a 0.9 NA objective at $\lambda = 532$ nm. Although our system employs a microscope objective with slightly lower numerical aperture and the coverslip on which the cells are plated introduces some optical aberrations (20), we believe the higher thresholds measured on the microscope setup described here are primarily due to the poor spatial beam quality of the Q-sw Nd:YAG laser. Q-sw Nd:YAG lasers with a Gaussian-coupled-resonator typically produce output beams that are multimode in nature ($M^2 > 2$) and prevents us from achieving diffraction-limited spot sizes in the focal plane (30). As a result, higher pulse energies are required to achieve the irradiances necessary for optical breakdown. In our system, we have a measured plasma threshold of 8 μJ. Assuming a threshold irradiance of $I_{th} = 7.8 \times 10^{10}$ W/cm^2 (19) implies that the laser beam radius in the focal plane is 0.738 μm for $\lambda = 532$ nm. This exceeds by nearly a factor of two the diffraction-limited spot size of 0.405 μm for a 0.8 NA objective. To further confirm that our threshold values were not due to a system error, we performed these measurements using an identical objective on a second laser-microscope system that utilized a Q-sw Continuum Surelite Nd:YAG laser (15,16) and obtained similar values for the plasma threshold (Continuum, Santa Clara, CA).

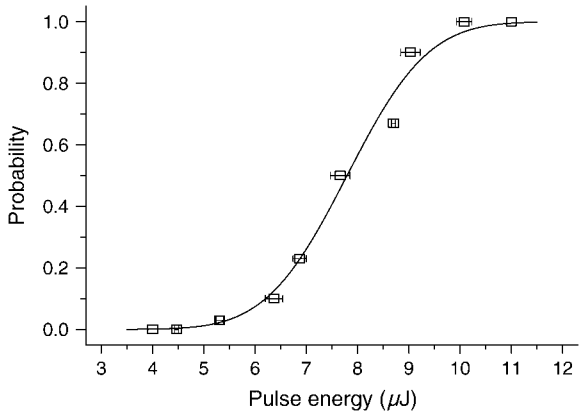

FIGURE 2 Probability of plasma incidence as a function of laser pulse energy with Gaussian error function fit.

Time-resolved imaging

Fig. 3 is a series of time-resolved images of the cell lysis process in a culture with surface density of 1000 cells/mm^2 produced at a pulse energy of 24 μJ corresponding to 3× the plasma threshold. Our image series follows the well-known evolution of an optical breakdown process starting with plasma formation, followed by shock wave propagation and finally cavitation bubble formation, expansion, and collapse (31). The plasma initiation, growth, and decay were complete within 25–30 ns after the arrival of the laser pulse. Close examination of Fig. 3 *a* reveals the formation of a shock wave resulting from the rapid plasma expansion. The shock wave propagation was followed until it passed outside the field of view (Fig. 3, *a–e*). Although the pressure amplitudes are considerable, approaching 480 MPa close to the irradiation site (20), the passage of the shock wave did not produce any visible disruption of the cell monolayer.

The plasma expansion resulted in cooling and ion-recombination thereby leading to the formation of a cavitation bubble within 25 ns after the laser pulse. The outer portions of the bubble appear dark due to the oblique angle of incidence of the illumination on the bubble surface that prevented transillumination. Fig. 3, *c–i*, reveals that cavitation bubble expansion is the primary mechanism of cell lysis

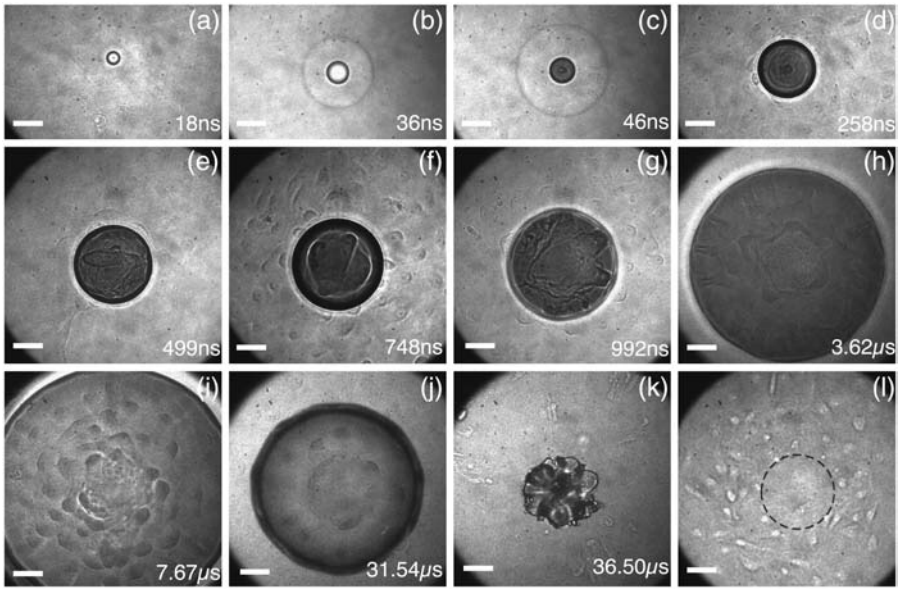

FIGURE 3 Time-resolved image series of the cell lysis process with cell surface density of 1000 cells/mm^2 at a pulse energy corresponding to 3× the threshold for plasma formation. Plasma formation, shock wave propagation, cavitation bubble dynamics, and development of the injury process are all clearly seen. Image times are as marked. Panel *l* is a phase contrast image and shows the cell sample post irradiation. Each 512 × 512 pixel image was binned 2 × 2 and the pixel intensity levels were adjusted in Adobe Photoshop (Adobe, San Jose, CA). Scale bar = 50 μm.

and several interesting features of this process can be seen in these images. At early times (35–200 ns) during the expansion of the cavitation bubble, cell injury is clearly visible within the central region of the bubble (Fig. 3, *d* and *e*). During this early expansion phase, cells that lie outside the bubble are lysed immediately upon arrival of the bubble wall. However, at some time point, (~200 ns at 3× plasma threshold for a surface density of 1000 cells/mm^2), arrival of the bubble wall does not result in additional cellular injury. Rather, further bubble expansion encompasses the cells without lysing them (Fig. 3 *h*). Another interesting feature is the transient deformation of the cells produced by the bubble expansion, evident in regions both inside and outside the bubble (Fig. 3, *g–i*). Remarkably, these cells appear to withstand this severe deformation without disruption. After reaching its maximum size, the bubble collapses quite rapidly, within 1–2 μs as seen in Fig. 3 *j*. Fig. 3 *k* shows the breakup of the bubble upon collapse. Close examination reveals that the cells surrounding the site of bubble collapse are deformed in a direction away from the center of the bubble. This may indicate the presence of radial fluid flow away from the center of the bubble collapse. The bubble collapse did not extend the zone of cell lysis but did clear any cellular debris present within the lysis zone. As a result, the lysis process results in a well-defined area around the irradiation site that is cleared of both cells and cellular debris (Fig. 3 *l*) that we define as the zone of cellular injury.

To examine whether the distance between the focal volume of the pulsed laser microbeam and the cell monolayer would affect the dynamics of the cell lysis process, we performed time-resolved imaging with a separation distance $s = 400$ μm, as opposed to $s = 10$ μm, between the focal plane of the laser microbeam and the cell monolayer. Fig. 4 shows the results of one such experiment at a pulse energy of 24 μJ corresponding to 3× threshold. Fig. 4 *a*, taken 14.4 μs after the laser pulse delivery, shows clearly that although bubble expansion produces significant cell deformation it does not produce cell lysis. However, in Fig. 4, *b* and *c*, taken at delay times of 29.4 and 32.4 μs, respectively, we see that cavitation bubble collapse, jet formation, and subsequent radial outflow of fluid results in the lysis of cells in the central region. Moreover, in Fig. 4 *c*, cell lysis can be observed in regions outside the collapsing bubble, due presumably to mechanical effects produced by the hydrodynamics associated with bubble collapse and jet formation.

Cavitation bubble dynamics

The temporal evolution of the cavitation bubble size was measured from a sequence of time-resolved images and

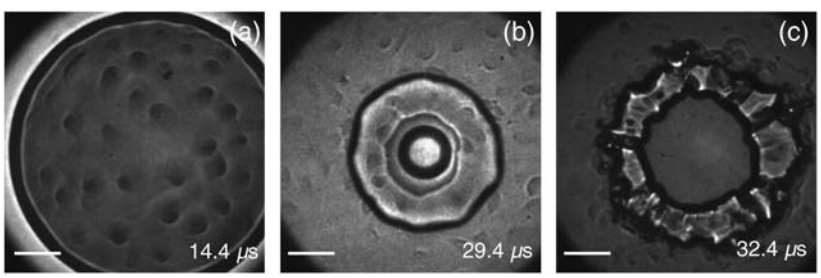

FIGURE 4 Cell lysis produced by cavitation bubble formation 400 μm above a cell monolayer with a surface density of 1000 cells/mm^2. (*a*) Image of an expanding cavitation bubble at 14.4 μs showing deformed, but intact, cells below the bubble. Images of bubble collapse at (*b*) 29.4 and (*c*) 32.4 μs, respectively, show cell lysis due to jet formation and radial outflow. The central region below the bubble has been cleared of cells. In panel *c*, cell lysis can also be observed outside the bubble. Scale bar = 50 μm.

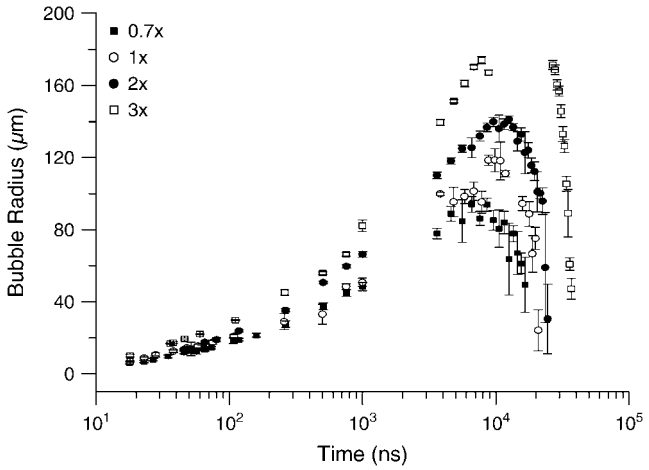

FIGURE 5 Cavitation bubble dynamics for pulse energies corresponding to 0.7×, 1×, 2×, and 3× the threshold for plasma formation. Each data point represents the average of three images.

shown in Fig. 5 for pulse energies corresponding to 0.7×, 1×, 2×, and 3× the threshold for plasma formation. A minimum of three images were used to calculate the average and standard deviation for each data point shown. It is important to note that the cavitation bubble dynamics are not influenced by the cell surface density. The values for maximum bubble radius R_{max} and oscillation time T_{osc} are of particular interest and are presented in Table 1. This case of inertially controlled bubble growth was considered by Lord Rayleigh, who derived the following expression relating the maximum cavitation bubble radius to the collapse time T_{col} as (32)

$$R_{max} = \frac{T_{col}}{0.915}\left[\frac{(p_\infty - p_v)}{\rho}\right]^{1/2}, \quad (2)$$

where ρ is the density of the liquid (1000 kg/m^3), p_∞ is the static pressure of the surrounding liquid, and p_v is the vapor pressure of the liquid (2330 Pa at 20°C). Our experimentally obtained values for R_{max} and T_{col} ($\equiv T_{osc}/2$) are consistent with Eq. 2. The energy of a hemispherical bubble E_B is given by

$$E_B = \frac{2}{3}\pi(p_\infty - p_v)R_{max}^3. \quad (3)$$

Substitution of Eq. 2 into Eq. 3 allows the bubble energy to be expressed in terms of the cavitation bubble parameters as

$$E_B = \frac{2}{3}\pi\rho\left(\frac{0.915}{T_{col}}\right)^2 R_{max}^5. \quad (4)$$

The bubble energy calculated using Eq. 4, as well as the percentage of the laser pulse energy transduced into bubble energy [$(E_B/E_p) \times 100$], are also presented in Table 1.

The radial position of the bubble wall during the cavitation bubble expansion was fit to the function $R_B(t) = [a + (b/\ln t)]^2$ with $R_B(t)$ being the bubble radius as a function of time and a and b being the fit parameters. This analytic expression was found to fit all the data series with regression coefficients >0.99 (Table Curve, Systat Software, Richmond, CA). An example of the raw data and curve fit for pulse energies of 5.6 and 24 μJ (0.7× and 3× threshold) is shown in Fig. 6 *a* over the time interval of 0–10 μs.

Velocities of the cavitation bubble expansion, as determined by differentiation of the analytic curve fits, are shown for all pulse energies in Fig. 6 *b*. It is seen that the maximum bubble expansion velocities increased with the laser pulse energy. Although the initial bubble expansion velocities are high, ranging between 320 and 510 m/s, they rapidly decrease to 18–32 m/s at 1 μs. The zone of cellular injury shown in Fig. 3 *l* is defined by the region around the irradiation site that was denuded of cells.

We determined the average size of the injury zone by measuring the radius of the cellular injury zones produced at 8–10 irradiation sites. In some instances the zone of cell lysis was elliptical and the radius of a circle of equivalent area was used instead. These results revealed that although the cavitation bubble dynamics are not affected by the cell surface density in the cell culture, the resulting zone of cell lysis is. The radial size of cellular injury as a function of pulse energy is shown in Table 1 for surface densities of 600 and 1000 cells/mm^2. For both surface densities, the zone of cellular injury was much smaller than the maximum cavitation bubble size. Specifically cell cultures with a surface density of 600 cells/mm^2, which had lysis zones that were consistently larger than cultures of 1000 cells/mm^2, had lysis zones with average radii of 29, 40, 45, and 63 μm for 0.7×, 1×, 2×, and 3× threshold, respectively, while the corresponding maximum cavitation bubble radii are 80, 120, 140, and 200 μm.

TABLE 1 Laser pulse energy (E_p), maximum cavitation bubble radius (R_{max}), oscillation time (T_{osc}), mechanical bubble energy (E_B), mechanical transduction efficiency (E_B/E_p), and radius of cell lysis for cultures with a cell surface density of 1000 cells/mm^2 (R_{inj}^{1000}) and 600 cells/mm^2 (R_{inj}^{600}) when using pulse energies corresponding to 0.7×, 1×, 2×, and 3× the threshold for plasma formation

	E_p [μJ]	R_{max} [μm]	T_{osc} [μs]	E_B [μJ]	E_B/E_p [%]	R_{inj}^{1000} [μm]	R_{inj}^{600} [μm]
0.7 × Threshold	5.6	95	17	0.18	3.2	19 ± 3	29 ± 2
1 × Threshold	8	118	21	0.34	4.3	23 ± 4	40 ± 4
2 × Threshold	16	140	25	0.57	3.6	30 ± 4	45 ± 5
3 × Threshold	24	200	37	1.66	6.9	36 ± 2	63 ± 6

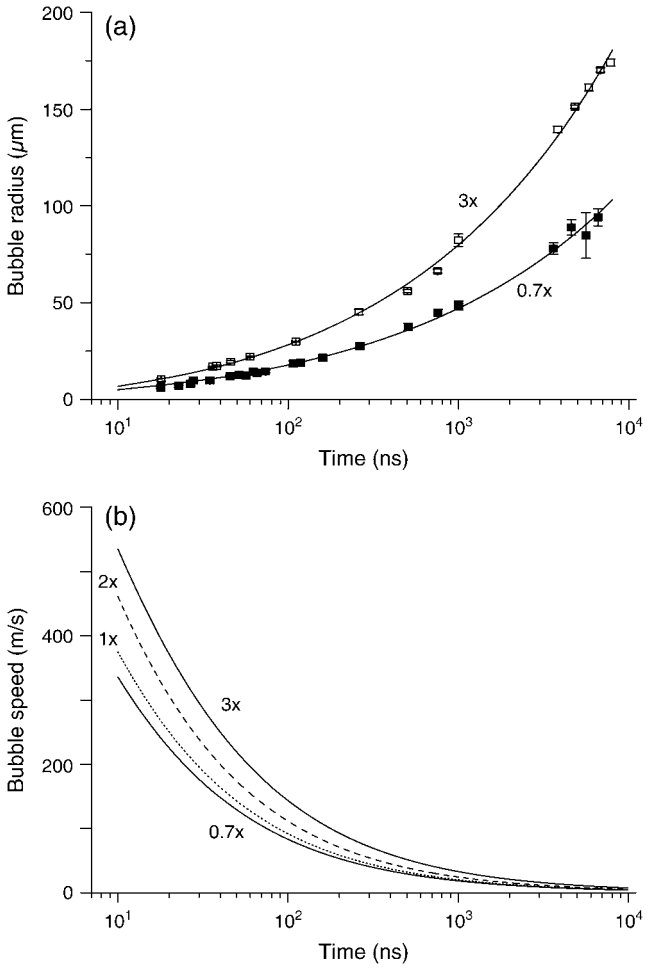

FIGURE 6 (*a*) Bubble expansion for 0.7× and 3× threshold pulse energy with curve fit. (*b*) Bubble velocities for pulse energies corresponding to 0.7×, 1×, 2×, and 3× the threshold for plasma formation as derived from curve fits.

Hydrodynamic modeling

Velocity and shear stress distributions produced by bubble expansion

The time-resolved images provide compelling evidence for the hypothesis that when the pulsed laser microbeam is focused immediately above the cell monolayer ($s = 10\ \mu$m), the primary agent for cell lysis and deformation is the dynamic shear stress produced by the fluid displacement associated with cavitation bubble expansion. To analyze these hydrodynamics we consider the model problem depicted in Fig. 7. We assume that the cell monolayer acts as a boundary and that the cells are subject to shear stress due to movement of fluid parallel to this boundary. We consider the fluid motion at locations outside the expanding bubble and define a geometry in which the origin is located at the site of the laser focus immediately above the cell monolayer with z and r being the vertical and radial axes, respectively. The transient external fluid velocity $V_\infty(r, t)$ produced by the cavitation

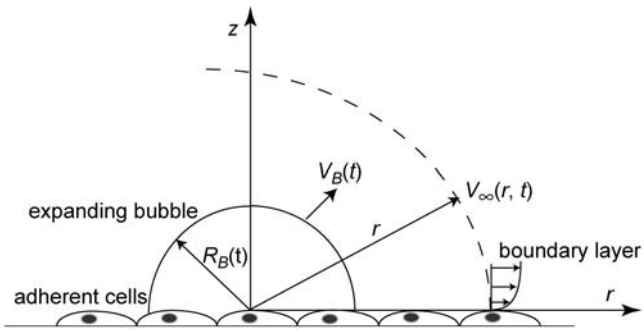

FIGURE 7 Schematic of model problem for hydrodynamic analysis. Figure not to scale.

bubble expansion is determined by applying conservation of mass for an incompressible fluid in spherical coordinates as

$$V_\infty(r,t) = V_B(t)\left[\frac{R_B(t)}{r}\right]^2, \tag{5}$$

where $R_B(t)$ and $V_B(t)$ are the time-varying position and velocity of the hemispherical bubble wall, respectively. Thus, by using experimental data for both $R_B(t)$ and $V_B(t)$, samples of which were shown in Fig. 6, we can obtain $V_\infty(r, t)$ at any desired radial location before the arrival of the bubble wall.

Of course, Eq. 5 is valid only at locations sufficiently removed from the boundary presented by the cell monolayer (and underlying glass coverslip) because the standard no-slip boundary applies at the boundary ($z = 0$). This results in the formation of a thin fluid layer proximal to the cell monolayer in which the fluid velocity varies as a function of both z and t. To examine the velocity distribution within this boundary layer, we first consider the results of Stokes' first problem for one-dimensional planar impulsive flow with a constant external velocity V_∞ (33). This translates to a boundary layer problem with the initial condition $V_\infty(z,\ t \le 0) = 0$ and boundary conditions $V(z = 0, t) = 0$ and $V(z \to \infty, t) = V_\infty$. The solution to this problem is given by (33)

$$V(z,t) = V_\infty \operatorname{erf}\left(\frac{z}{2\sqrt{\nu t}}\right), \tag{6}$$

where erf(x) is the error function defined earlier in connection with Eq. 1 and ν is the kinematic viscosity of the culture medium (0.896×10^{-6} m^2/s).

In contrast to Stokes' first problem where V_∞ is constant in both space and time, in our problem V_∞ varies with both radial position and time, that is, $V_\infty = V_\infty(r, t)$. Moreover, we have boundary layer flow in a spherical rather than a one-dimensional planar geometry. This latter issue regarding boundary layer curvature can be ignored so long as we consider radial positions much larger than the boundary layer thickness, i.e., $r \gg \delta$. The case of a external velocity that varies with both space and time changes the boundary condition at $z \to \infty$ to $V(r, z \to \infty, t) = V_\infty(r, t)$. For this case, the velocity distribution in the boundary layer can be determined by temporally convolving the result of Stokes'

first problem given by Eq. 6 with the temporal variation of $V_\infty(r, t)$ given by the experimental data via Eq. 5. This approach to constructing the solution to a problem possessing a boundary condition that varies with both space and time from the response of the system to a step function is known as Duhamel's integral (34). This situation has been considered previously by several investigators including Lokhandwalla and Sturtevant who provide the result (35)

$$V(r,z,t) = \int_0^t \frac{\partial V_\infty(r,t')}{\partial t'} \mathrm{erf}\left[\frac{z}{2\sqrt{\nu(t-t')}}\right] dt'. \quad (7)$$

From Eq. 7, the wall shear stress experienced by the cells $\tau_w(r, z = 0, t)$ can be obtained at any radial position r for the time interval $0 \le t \le t^*$, where t^* is the time of arrival of the bubble wall at position r using

$$\tau_w(r,t) = \rho\nu\left(\frac{\partial V}{\partial z}\right)\Big|_{z=0} = \rho\sqrt{\frac{\nu}{\pi}}\int_0^t \frac{\partial V_\infty(r,t')}{\partial t'}\frac{dt'}{\sqrt{t-t'}}, \quad (8)$$

where ρ is the density of the culture medium (1000 kg/m^3). Equations 7 and 8 provide a complete description of the velocity field and wall shear stress at any location before the arrival of the bubble wall. It is important to realize that the predictions given by these equations result simply from the application of the conservation of mass and momentum to the experimental data and contain no adjustable parameters.

Given the availability of these modeling results, we are interested in examining possible correlations between the characteristics of the fluid field and the resulting zone of cellular injury. The natural place to look are the velocity profiles and wall shear stresses experienced at the radial positions corresponding to the edge of the injury zone $r = R_{inj}$ at the time of arrival of the cavitation bubble wall t^*. Fig. 8 presents velocity profiles within the boundary layer at the time of arrival of the bubble wall at the radial location corresponding to the edge of the zone of cellular injury for pulse energies corresponding to 0.7×, 1×, 2×, and 3× threshold within a cell culture with surface density of 1000 cells/mm^2 i.e., $V(r = R_{inj}^{1000}, z, t = t^*)$. The distance at which the fluid velocity is equal to 99% of the external fluid velocity is known as the boundary layer thickness and for the cases shown in Fig. 8, ranges from 1.04–1.25 μm. The experimental data and hydrodynamic model results are summarized in Table 2 for cell densities of 1000 and 600 cells/mm^2. Due to only small differences in bubble velocities for 0.7× and 1× threshold (see Fig. 6 *b*), the boundary layer velocity profile for both is also fairly similar, with the external fluid velocity being slightly less for 1× threshold at $r = R_{inj}$. This is due to the larger value of $R_{inj} = 23$ μm at 1× threshold versus 19 μm for 0.7× threshold.

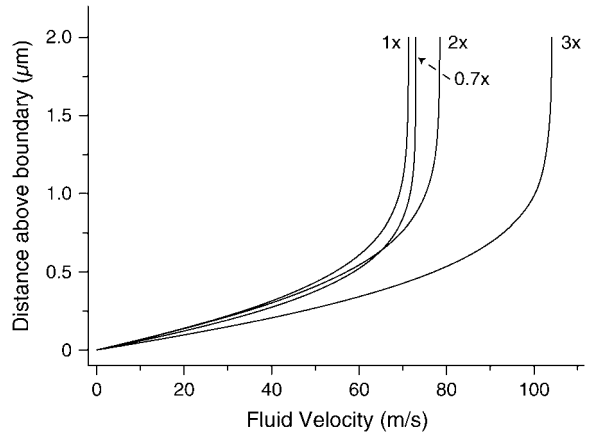

FIGURE 8 Velocity profile as a function of distance above cell monolayer at $r = R_{inj}$ of 19, 23, 30, and 36 μm for pulse energies corresponding to 0.7×, 1×, 2×, and 3× the threshold for plasma formation, respectively.

In Fig. 9 we provide the temporal profile of the wall shear stress $\tau_w(t)$ at different radial positions for a pulse energies corresponding to 1× and 2× the threshold for plasma formation. The temporal shape of the shear stress is similar regardless of location; that is, the peak shear stress is reached after a relatively rapid rise followed by a more gradual decline. The time intervals over which the shear stress is provided increases with radial position and simply reflects the longer time necessary for the bubble front to arrive at that location, after which time the model is no longer valid. As expected, the peak shear stress decreases with increasing radial position. In Fig. 10, *a* and *b*, we plot the wall shear stress as a function of time at the radial location demarcating the zone of cell lysis $\tau_w(r = R_{inj}, t)$ for pulse energies corresponding to 0.7×, 1×, 2×, and 3× threshold for cell surface density of 1000 and 600 cells/mm^2, respectively. For a given cell density, the similarity of the temporal profiles of the wall shear stress at R_{inj} is truly remarkable, especially given the more-than-fourfold variation in laser pulse energy. Moreover, the peak wall shear stress necessary to cause lysis does not appear to vary systematically with the laser pulse energy. Specifically, the peak wall shear stress at the rim of the zone of cell lysis ($r = R_{inj}$) lies in a narrow range of 180–220 kPa for a cell density of 1000 cells/mm^2 (Fig. 10 *a*), and 60–84 kPa for a cell density of 600 cells/mm^2 (Fig. 10 *b*). Thus, the minimum peak shear stress necessary to cause lysis for the cell density of 1000 cells/mm^2 is ~3× higher compared to 600 cells/mm^2.

The above hydrodynamic analysis of our experimental results strongly supports the hypothesis that for a specific cell surface density the spatial extent of cellular injury is determined by the maximum shear stress produced by the cavitation bubble expansion. To aid in examining this hypothesis for both cell surface densities examined, we provide in Fig. 11 the spatial distribution of the peak shear stress generated by the cavitation bubble expansion at pulse energies corresponding to 0.7×, 1×, 2×, and 3× threshold. Note that the shear stress predictions are based on the experimental measurements of the cavitation bubble dynamics $R_B(t)$ that are known to greater precision than the

TABLE 2 Summary of hydrodynamic data and analysis providing the radius of cell lysis (R_{inj}), bubble arrival time at R_{inj} (t^*), the external fluid velocity (V_∞) and boundary layer thickness (δ) at $r = R_{inj}$ and $t = t^*$, and the peak wall shear stress $\tau_{w,peak}$ for pulse energies corresponding to 0.7×, 1×, 2×, and 3× the threshold for plasma formation

		Experimental data		Model predictions		
Cell density [#/mm^2]	Pulse energy E_p [μJ]	Zone of cell injury R_{inj} [μm]	Bubble arrival time t^* [ns]	External fluid velocity $V_\infty(R_{inj}, t^*)$ [m/s]	Boundary layer thickness $\delta(R_{inj}, t^*)$ [μm]	Peak wall shear stress $\tau_{w,peak}$ [kPa]
1000	5.6	19 ± 3	115	73	1.04	189 ± 61
	8	23 ± 4	139	71	1.16	180 ± 64
	16	30 ± 4	159	79	1.25	198 ± 54
	24	36 ± 2	164	104	1.23	219 ± 24
600	5.6	29 ± 2	303	40	1.74	81 ± 13
	8	40 ± 4	513	31	2.30	60 ± 14
	16	45 ± 5	418	44	2.08	84 ± 23
	24	63 ± 6	568	47	2.38	72 ± 16

measured experimental variation in R_{inj}. As a result, the uncertainty in the peak shear stress experienced by the cells is dictated by the observed variation in the radial size of the zone of cell lysis R_{inj} rather than the uncertainties inherent in the measurement of the bubble dynamics $R_B(t)$. Given the steep variation in the peak shear stress with radial location, a small uncertainty in the measurement of R_{inj} leads to a rather large uncertainty in the peak shear stress. This is shown in Table 2 where the zones of cellular injury for each cell surface density is listed along with the peak wall shear stress as a function of pulse energy. We also present the corresponding external fluid velocity $V_\infty(r = R_{inj}, t = t^*)$ and boundary layer thickness δ at the edge of the zone of cell injury at the time of bubble arrival.

DISCUSSION

Role of plasma formation and shock wave propagation on cell injury

Time-resolved imaging provides a precise means to visualize and quantify the effects of optical breakdown on adherent cells. Our microscope setup provides an image resolution of ≈1 μm while the ICCD camera provides a maximum temporal resolution of 0.5 ns. This combination of high spatial and temporal resolutions enables accurate, high-speed imaging of the cell lysis process. The plasma is visible at the earliest time point of 0.5 ns and its evolution could be followed until the plasma luminescence ceased (25–30 ns). While the high temperature plasma and its explosive expansion can cause cell vaporization, we could not visualize this process due to the plasma luminescence. The plasma expansion results in the radiation of a shock wave with pressure amplitudes approaching 480 MPa (20). However, no cellular injury resulting from the shock wave propagation through the cell layer is observed and highlights the ability of these cells to withstand shock. This finding is consistent with other studies that found no evidence of cellular injury by laser-induced pressure waves alone (23,36).

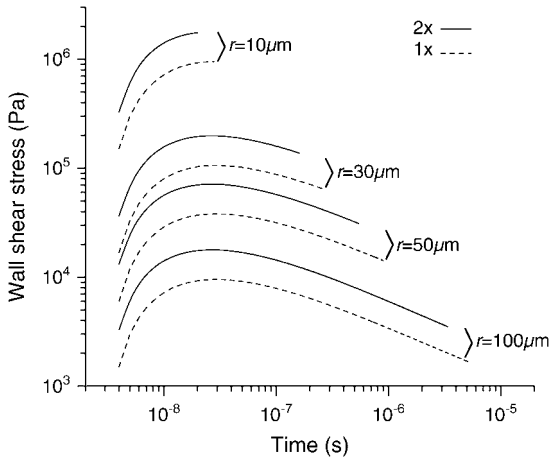

FIGURE 9 Temporal shear stress profile as a function of radial position at 2× threshold. The shear stress is calculated until the time of arrival of the bubble rim at that radial position.

Role of cavitation bubble expansion and shear stress on cell injury

Time-resolved imaging provides evidence that the fluid flow resulting from cavitation bubble expansion is the primary agent of cellular injury. Cell lysis is initiated at the site of plasma formation and propagates outwards with the bubble expansion. We can infer that cavitation bubble expansion produces cell membrane disruption and cell lysis rather than merely cell detachment because cellular debris was consistently observed proximal to the irradiation site and intact cells were never observed to be floating in the culture medium after laser pulse delivery. Previous work by the Allbritton group has also shown that laser-induced plasma formation with pulse energies similar to those used here causes cell membrane disruption (9,10).

The production of laser-induced breakdown at a separation distance $s = 10$ μm above the cell monolayer led to cavitation bubble formation whose proximity to the monolayer enhanced the damage potential of the resulting hydrodynamic flow. Cell lysis occurred rapidly and the zone of cell lysis was fully developed within 200 ns for 1000 cells/mm^2

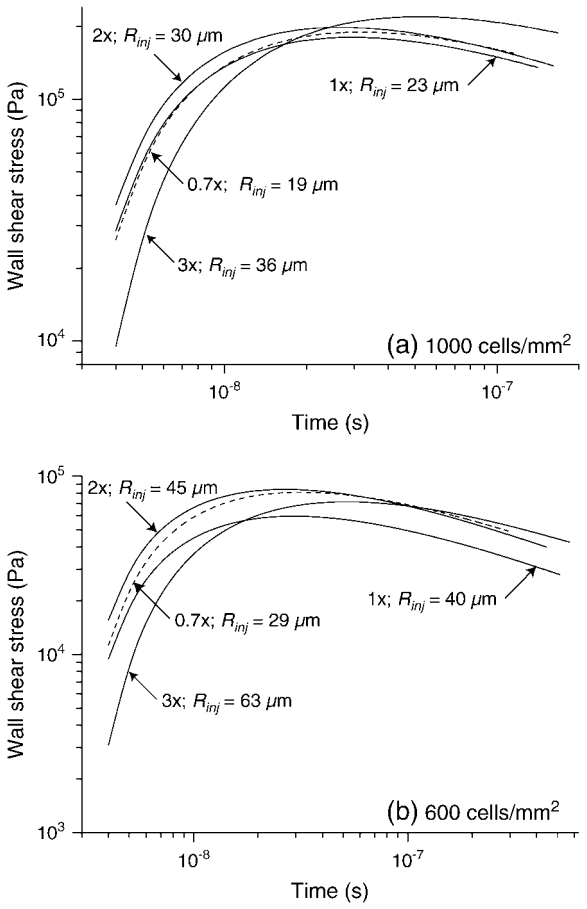

FIGURE 10 (*a*) Temporal profiles of the wall shear stress at $r = R_{inj}$ of 19, 23, 30, and 36 μm corresponding to irradiation at pulse energies of 0.7×, 1×, 2×, and 3× the threshold for plasma formation, respectively, for a cell surface density of 1000 cells/mm^2. (*b*) Temporal profiles of the wall shear stress at $r = R_{inj}$ of 29, 40, 45, and 63 μm corresponding to irradiation at 0.7×, 1×, 2×, and 3× the threshold for plasma formation, respectively, for a cell surface density of 600 cells/mm^2.

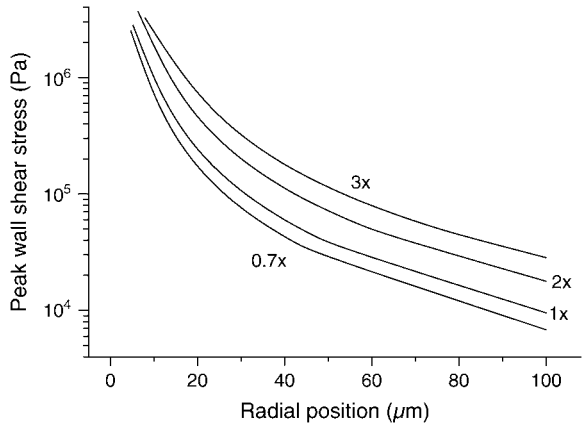

FIGURE 11 Peak wall shear stress $\tau_{w,peak}$ as function of radial position at pulse energies 0.7×, 1×, 2×, and 3× the threshold for plasma formation.

and within 600 ns for 600 cells/mm^2 at 3× threshold pulse energy. Thereafter bubble expansion did not result in cell lysis. The bubble velocity as determined from the time-resolved images revealed velocities in the range of 320–510 m/s at early times that rapidly decreased to 31–104 m/s at the edge of the injury zone, as shown in Fig. 6 *b* and Table 2. Adherent cells at the border of the zone of cell lysis remained intact but underwent significant transient deformation from the large shear stresses associated with the cavitation bubble dynamics. Thus, depending on the location of the cell, the shear stresses could either cause lysis or, for larger radial locations, transient deformation of the cell body.

These results are consistent with those of Wolfrum and co-workers who examined the effect of pressure wave-excited contrast agent bubbles on rat kidney fibroblast cells (37). Using time-resolved imaging, the authors observed that under the action of pressure waves, contrast agent bubbles near cells expanded from a diameter of 2–62 μm within 3 μs. Although the bubbles did not cause cell lysis during expansion, they were observed to produce transient deformation of the cells. Cell lysis or rupture was only observed upon bubble collapse. The characteristic bubble expansion velocities (<10 m/s; determined from Fig. 2 of Wolfrum) and bubble diameters (<60 μm) were significantly smaller than those produced in our study. These factors limited the damage potential of the bubble expansion in the Wolfrum study.

Our hydrodynamic model provides a means to determine the spatiotemporal evolution of both the fluid velocity and wall shear stress. This enables a correlation between the observed cellular effects and the fluid flow characteristics. We assume that the bubble-cell interactions were mediated by a thin fluid layer between the expanding bubble and the cell monolayer at all times (38,39). This assumption is borne out by the fact that even cells that were encompassed by the bubble (Fig. 3, *h* and *i*) underwent significant deformation, a result only possible due to the presence of a thin fluid layer between the bubble and cells. It was also seen that regardless of the laser pulse energy, PtK_2 cells cultured at a surface density of 1000 cells/mm^2 remained adherent even when subject to transient wall shear stresses approaching 180–220 kPa, while those cultured at a surface density of 600 cells/mm^2 only withstood transient wall shear stresses approaching 60–84 kPa. The fact that this range of wall shear stress does not vary systematically with laser pulse energy but with cell surface density suggests the presence of a critical wall shear stress for cell lysis on the nanosecond timescale. Moreover, the finding that the critical shear stress increases with increasing cell surface density suggests that the higher cell surface density may promote changes in cell-cell or cell-substratum interactions that provide for greater mechanical resilience (40–42).

In addition, we observed that adherent cells had the ability to withstand large shear stresses without visible damage. Even though the peak wall shear stress experienced by cells at $r =$ 100 μm were much lower than those on the border of the lysis zone, they were still in the 7–28 kPa range (Fig. 11). Visual

examination of the cells surrounding the lysis zone 24 h post-irradiation revealed their continued viability and proliferation. Recent work modeling fluid flow during hemolysis of red blood cells in suspension when exposed to shock wave lithotripsy revealed that cells can withstand high spatial velocity gradients if exposures were limited to nanosecond timescales (35). Our imaging results and hydrodynamic analysis show that interactions between laser-generated cavitation bubbles and adherent cells are governed by similar considerations, with cells capable of sustaining large shear stresses over short time exposures. It is possible that these high shear stresses cause other physiological changes within cells including transient membrane permeabilization, spikes in Ca^{2+} signaling, detachment of focal adhesion sites, disruption of cytoskeleton, etc. Investigation of such changes using fluorescence assays is currently underway.

Role of bubble collapse on cell injury

We found no significant contribution of the bubble collapse to cellular injury when focusing the pulsed laser microbeam at a separation distance of $s = 10$ μm above the cell monolayer. This is an interesting observation since cavitation bubble collapse is a well-known damage mechanism ranging from the pitting of ship propellers and vacuum pumps to the breakup of kidney stones in shock wave lithotripsy (32,43). In an extensive study examining the mechanisms of intraocular surgery using Nd:YAG laser pulses, Vogel and co-workers studied several different irradiation geometries, all using relatively low numerical apertures, to determine the specific contributions of plasma formation and cavitation bubble dynamics to the injury process (23). For cases where the laser was focused above an ex vivo sample of corneal tissue (an irradiation geometry similar to our experiments), it was shown that for a constant laser pulse energy the extent of damage was dependent upon the parameter γ, defined as the ratio between the separation distance s and the maximum cavitation bubble radius R_{max}. In these cases, images taken after the laser-tissue interaction revealed the corneal surface to be punctured with a region surrounding the puncture site denuded of corneal endothelial cells. This latter feature is similar to the zone of cell lysis observed in our study.

Vogel and co-workers implicated the impact of a liquid jet during cavitation bubble collapse as the cause for puncture of the corneal endothelium and stroma while the region of denuded cells was attributed to the radial outflow of the jet after impact (23). This is in contrast with our results obtained at a separation distance $s = 10$ μm that clearly demonstrate cell lysis to occur during the cavitation bubble expansion and not during the bubble collapse. In the Vogel study, the smallest value of γ ($\equiv s/R_{max}$) tested was 0.15. Due to the large pulse energies and low focusing angles used, this small γ-value was accomplished with a 100 μm separation distance between the focal plane of the laser beam and the tissue boundary. This significant distance from the surface of the cells reduces both the fluid velocity and the shear stress to which the cells are exposed upon the cavitation bubble expansion. Moreover, this greater distance allows for coherent and focused jet formation upon bubble collapse.

By contrast, in our experiments the site of plasma formation was 10 μm above the cell monolayer. This not only results in smaller values of $\gamma = 0.06$–0.13 but also exposes the cells to the maximal effects of the shear stresses produced by the rapid bubble expansion resulting in cell lysis. Once the cells were lysed, nothing viable remained in the central region that would be susceptible to the jet impact and radial outflow produced upon bubble collapse. Moreover, the small γ-value results in the production of a hemispherical bubble and results in a bubble collapse and breakup that likely reduces the effects of liquid jet impact (44).

Of related importance are studies of shock wave lithotripsy that have shown bubble collapse to be the mechanism of cell injury. A time-resolved study by Ohl and Wolfrum on the effects of shock-wave excited cavitation bubbles on adherent cells demonstrated that bubble collapse caused cell detachment and membrane permeabilization (45). Bubble sizes and collapse times in the Ohl study are comparable to those produced by irradiation at 3× threshold in our study. However, since bubble generation in the Ohl study is shock wave-induced, the time and location of bubble formation could not be controlled. This may have led to the production of fewer bubbles in the immediate proximity of the cells—thereby reducing their exposure to the hydrodynamic effects during bubble expansion and increasing cell survival.

Taken together, the results of these earlier studies and our findings provide strong evidence that the site of bubble generation is a critical factor determining whether cell injury occurs during the expansion or collapse phase of the cavitation bubble dynamics. Our studies of optical breakdown produced at larger separation distances from the boundary confirm this. Plasma formation at a pulse energy 3× plasma threshold using a separation distance of $s = 400$ μm resulted in $\gamma = 1.6$. In this case, the fluid flow generated during bubble expansion produced cell deformation but not cell lysis (Fig. 4 *a*). Instead, the asymmetric bubble collapse produced a coherent jet directed toward the cells that concentrated energy away from the bubble. Cell lysis resulted from the jet impact and subsequent radial outflow of the fluid jet (Fig. 4, *b* and *c*). These experiments resulted in zones of cell injury significantly larger than those produced by the bubble expansion when smaller γ-values were used. This increased damage zone is most similar to the conditions used in studies of intraocular laser surgery and shock wave lithotripsy-induced injury, described by both Vogel and Ohl (23,45).

Effect of pulse energy on cell injury

The delivery of subthreshold pulse energies also allowed the investigation of the potential use of low energy pulses for

single cell lysis. Our results show that both bubble size and bubble energy are reduced significantly when using subthreshold pulse energies. As shown in Table 1, a 30% reduction in pulse energy from 1× to 0.7× threshold results in a 20% reduction in bubble size and a 50% reduction in bubble energy. For the cultures with a surface density of 1000 cells/mm^2, this resulted in the lysis of only 2–3 cells. It should be noted that our use of a multimode laser beam resulted in higher plasma threshold energies than in cases where beams of better spatial quality were used (19). Reductions in plasma threshold energy can also be accomplished using a multimode beam in conjunction with a spatial filter (46), microscope objectives with higher numerical aperture, or shorter laser pulse durations. The use of laser parameters that result in lower plasma threshold energies will provide for further increases in precision by accomplishing further reductions in both the plasma and bubble energies.

These results are also suggestive of the injury mechanism during cell microsurgery wherein intracellular organelles are irradiated with subthreshold nanosecond laser pulses focused through a 1.3 NA objective (15,47,48). In these cases, the laser is operated at a 10–20 Hz repetition rate and the cell is typically exposed to tens to thousands of pulses. This procedure produces intracellular injury, even in the absence of an endogenous absorption, without compromising cell survival. We believe that laser-induced breakdown provides a viable mechanism for injury in these cases. At subthreshold pulse energies, plasma formation may only be induced by a small fraction of the delivered laser pulses. In addition, when formed, the plasma energy density would be extremely low and result in a minimal transduction of incident laser pulse energy into bubble energy. Thus, the bubble size would be small, and the injury may be confined to the volume of the plasma itself, thereby providing for higher rates of cell survival.

CONCLUSION

Cell lysis produced by Q-sw pulsed laser microbeam irradiation at $\lambda = 532$ nm in cell monolayers cultured at densities of 600 and 1000 cells/mm^2 was investigated using time-resolved imaging and hydrodynamic analysis with pulse energies of 5.6–24 μJ. The well-known sequence of plasma formation, shock wave propagation, and cavitation bubble formation, expansion, and collapse was observed with high temporal and spatial resolution. Cavitation bubble expansion and not collapse was seen to be the primary agent of cell lysis when the pulsed laser microbeam was focused at a separation distance of $s = 10$ μm above the cell monolayer. The lysis process is extremely rapid, reaching completion within 200 and 600 ns at the highest pulse energy tested for cell monolayers with surface densities of 1000 and 600 cells/mm^2, respectively. Maximum bubble sizes were significantly larger than the cell injury zones, indicating that as the bubble expansion slowed, the associated wall shear stresses were not sufficient to cause lysis. Images also revealed the ability of cells to remain adherent after being subject to strong transient deformation. We also confirmed that production of cavitation bubbles at separation distances of $s = 400$ μm above the cell monolayer results in larger zones of cell injury that are produced upon cavitation bubble collapse and not expansion. Thus, with the proper control of the pulse energy and location of the focal volume of the pulsed laser microbeam, it is possible to precisely control both the extent and temporal evolution of cellular injury.

Hydrodynamic analysis based on the measured time evolution of the cavitation bubble growth revealed that the time-resolved wall shear stress at a particular radial position increased rapidly to a maximum value followed by a more gentle decay. This analysis revealed that cell monolayers cultured at surface densities of 1000 cells/mm^2 can withstand transient shear stresses of 180–220 kPa without damage or detachment, whereas peak shear stresses are in the range of 7–28 kPa at 100 μm from the site of irradiation. Cell lysis zones in monolayers cultured at a surface density of 600 cells/mm^2 were substantially larger and these cells were found capable of withstanding peak shear stresses of only 60–84 kPa. This finding suggests that reductions in the cell surface density may result in changes in cell-cell or cell-substratum interactions that make them more susceptible to lysis by the laser-generated shear stresses.

The authors thank Roger Kamm, Bora Mikić, and Alfred Vogel for valuable discussions and Carole Hayakawa for computational expertise. We acknowledge support from the National Institutes of Health via the Laser Microbeam and Medical program No. P41-RR-01192, Bioengineering Research Partnership program No. R01-RR-14892, and No. R01-EB04436.

REFERENCES

1. Berns, M. W., J. Aist, J. Edwards, K. Strahs, J. Girton, P. McNeill, J. B. Rattner, M. Kitzes, M. Hammer-Wilson, L.-H. Liaw, A. Siemens, M. Koonce, S. Peterson, S. Brenner, J. Burt, R. Walter, P. J. Bryant, D. van Dyk, J. Coulombe, T. Cahill, and G. S. Berns. 1981. Laser microsurgery in cell and developmental biology. *Science.* 213:505–513.
2. Khodjakov, A., R. W. Cole, B. F. McEwen, K. F. Buttle, and C. L. Rieder. 1997. Chromosome fragments possessing only one kinetochore can congress to the spindle equator. *J. Cell Biol.* 136:229–240.
3. Greulich, K. O., and G. Pilarczyk. 1998. Laser tweezers and optical microsurgery in cellular and molecular biology. Working principles and selected applications. *Cell. Mol. Biol.* 44:701–710.
4. Greulich, K. O., G. Pilarczyk, A. Hoffmann, G. M. Z. Hörste, B. Schäfer, V. Uhl, and S. Monajembashi. 2000. Micromanipulation by laser microbeam and optical tweezers: from plant cells to single molecules. *J. Microsc.* 198:182–187.
5. Lin, C. P., M. W. Kelly, S. A. B. Sibayan, M. A. Latina, and R. R. Anderson. 1999. Selective cell killing by microparticle absorption of pulsed laser radiation. *IEEE J. Sel. Topics Quantum Elec.* 5:963–968.
6. Pitsillides, C. M., E. K. Joe, X. Wei, R. R. Anderson, and C. P. Lin. 2003. Selective cell targeting with light-absorbing microparticles and nano-particles. *Biophys. J.* 84:4023–4032.
7. Palsson, B. O., M. R. Koller, and T. M. Eisfeld. 2003. Method and apparatus for selectively targeting specific cells within a mixed cell population. U.S. Patent No. 6534308B1.

8. Conn, P. M., editor. 2002. Laser capture in microscopy and microdissection. *In* Methods in Enzymology, Vol. 356. Academic Press, New York.
9. Sims, C. E., G. D. Meredith, T. B. Krasieva, M. W. Berns, B. J. Tromberg, and N. L. Allbritton. 1998. Laser-micropipette combination for single cell analysis. *Anal. Chem.* 70:4570–4577.
10. Meredith, G. D., C. E. Sims, J. S. Soughhayer, and N. L. Allbritton. 2000. Measurement of kinase activation in single mammalian cells. *Nat. Biotechnol.* 18:309–312.
11. Sims, C. E., and N. L. Allbritton. 2003. Single-cell kinase assays: opening a window onto cell behavior. *Curr. Opin. Biotechnol.* 14:23–28.
12. He, M., J. S. Edgar, G. D. M. Jeffries, R. M. Lorenz, J. P. Shelby, and D. T. Chiu. 2005. Selective encapsulation of single cells and subcellular organelles into picoliter- and femtoliter-volume droplets. *Anal. Chem.* 77:1539–1544.
13. Vogel, A., and V. Venugopalan. 2003. Mechanisms of pulsed laser ablation of biological tissue. *Chem. Rev.* 103:577–644.
14. Vogel, A., J. Noack, G. Hüttman, and G. Paltauf. 2005. Mechanisms of femtosecond laser nanosurgery of cells and tissues. *Appl. Phys. B.* 81: 1015–1047.
15. Kim, J. S., T. B. Krasieva, V. LaMorte, A. M. Taylor, and K. Yokomori. 2002. Specific recruitment of human cohesin to laser-induced DNA damage. *J. Biol. Chem.* 47:45149–45153.
16. Krasieva, T. B., C. F. Chapman, V. J. Lamorte, V. Venugopalan, M. W. Berns, and B. J. Tromberg. 1998. Cell permeabilization and molecular transport by laser microirradiation. *Proc. SPIE.* 3260:38–44.
17. Berns, M. W. 1976. A possible two-photon effect in vitro using a focused laser beam. *Biophys. J.* 16:973–977.
18. Calmettes, P. P., and M. W. Berns. 1983. Laser-induced multiphoton processes in living cells. *Proc. Natl. Acad. Sci. USA.* 80:7197–7199.
19. Venugopalan, V., A. Guerra III, K. Nahen, and A. Vogel. 2002. Role of laser-induced plasma formation in pulsed cellular microsurgery and micromanipulation. *Phys. Rev. Lett.* 88:078103.
20. Rau, K. R., A. G. Guerra III, A. Vogel, and V. Venugopalan. 2004. Investigation of laser-induced cell lysis using time-resolved imaging. *Appl. Phys. Lett.* 84:2940–2942.
21. Steinert, R. F., and C. A. Puliafito. 1985. The Nd:YAG Laser in Opthalmology: Principles and Clinical Applications of Photodisruption. W. B. Saunders, Philadelphia, PA.
22. Gabel, V. P., L. Neubauer, H. Zink, and R. Birngruber. 1985. Ocular side effects following Nd:YAG laser irradiation. *In* Neodynium:YAG Laser Microsurgery: Fundamental Principles and Clinical Applications, Vol. 25. R. M. Klapper, editor. Little, Brown, Boston. 137–149.
23. Vogel, A., P. Schweiger, A. Frieser, M. N. Asiyo, and R. Birngruber. 1990. Intraocular Nd:YAG laser surgery: light-tissue interaction, damage range and reduction of collateral effects. *IEEE J. Quantum Elec.* 26:2240–2260.
24. Vogel, A., M. R. C. Capon, M. N. Asiyo-Vogel, and R. Birngruber. 1994. Intraocular photodisruption with picosecond and nanosecond laser pulses: tissue effects in cornea, lens, and retina. *Invest. Ophthalmol. Vis. Sci.* 35:3032–3044.
25. Vogel, A., S. Busch, K. Jungnickel, and R. Birngruber. 1994. Mechanisms of intraocular photodisruption with picosecond and nanosecond laser pulses. *Lasers Surg. Med.* 15:32–43.
26. Juhasz, T., X. H. Hu, T. Laszlo, and Z. Bor. 1994. Dynamics of shock waves and cavitation bubbles generated by picosecond laser pulses in corneal tissue and water. *Lasers Surg. Med.* 15:91–98.
27. Juhasz, T., G. A. Kastis, C. Suárez, Z. Bor, and W. E. Bron. 1996. Time-resolved observations of shock waves and cavitation bubbles generated by femtosecond laser pulses in corneal tissue and water. *Lasers Surg. Med.* 19:23–31.
28. Vogel, A., R. J. Scammon, and R. P. Godwin. 1999. Tensile stress generation by optical breakdown in tissue: experimental investigations and numerical simulations. *Proc. SPIE.* 3601:191–206.
29. Vogel, A., K. Nahen, D. Theisen, and J. Noack. 1996. Plasma formation in water by picosecond and nanosecond Nd:YAG laser pulses. Part I: Optical breakdown at threshold and superthreshold irradiance. *IEEE J. Sel. Topics Quantum Elec.* 2:847–860.
30. Caprara, A., and G. C. Reali. 1992. Time resolved M^2 of nanosecond pulses from a Q-switched variable-reflectivity-mirror Nd:YAG laser. *Opt. Lett.* 17:414–416.
31. Vogel, A., S. Busch, and U. Parlitz. 1996. Shock wave emission and cavitation bubble generation by picosecond and nanosecond optical breakdown in water. *J. Acoust. Soc. Am.* 100:148–165.
32. Brennen, C. E. 1995. Cavitation and Bubble Dynamics. Oxford University Press, New York.
33. Schlichting, H. 1979. Boundary-Layer Theory. McGraw-Hill, Englewood Cliffs, NJ. 90–91.
34. Courant, R. E., and D. Hilbert. 1962. Methods of Mathematical Physics, Vol. II. Wiley-Interscience, New York.
35. Lokhandwalla, M., and B. Sturtevant. 2001. Mechanical haemolysis in shock wave lithotripsy (SWL): I. Analysis of cell deformation due to SWL flow-fields. *Phys. Med. Biol.* 46:413–437.
36. Sondén, A., B. Svensson, N. Roman, B. Brismar, J. Palmblad, and B. T. Kjellström. 2002. Mechanisms of shock wave induced endothelial cell injury. *Lasers Surg. Med.* 31:233–241.
37. Wolfrum, B., R. Mettin, T. Kurz, and W. Lauterborn. 2002. Observations of pressure-wave-excited contrast agent bubbles in the vicinity of cells. *Appl. Phys. Lett.* 81:5060–5062.
38. Bilek, A. M., K. C. Dee, and D. P. Gaber III. 2003. Mechanisms of surface-tension-induced epithelial cell damage in a model of pulmonary airway reopening. *J. Appl. Physiol.* 94:770–783.
39. Cooper, M. G., and A. J. P. Lloyd. 1969. The microlayer in nucleate pool boiling. *Int. J. Heat Mass Transfer.* 12:895–913.
40. Ryan, P. L., R. A. Foty, J. Kohn, and M. S. Steinberg. 2001. Tissue spreading on implantable substrates is a competitive outcome of cell-cell vs. cell-substratum adhesivity. *Proc. Natl. Acad. Sci. USA.* 98:4323–4327.
41. Boal, D. H. 2002. Mechanics of the Cell. Cambridge University Press, Cambridge, UK.
42. Chen, C. S., J. Tan, and J. Tien. 2004. Mechanotransduction at cell-matrix and cell-cell contacts. *Annu. Rev. Biomed. Eng.* 6:275–302.
43. Rink, K., G. Delacretaz, and R. P. Salathe. 1995. Fragmentation process of current laser lithotripters. *Lasers Surg. Med.* 16:134–146.
44. Vogel, A., W. Lauterborn, and R. Timm. 1989. Optical and acoustic investigation of the dynamics of laser-produced cavitation bubbles near a solid boundary. *J. Fluid Mech.* 206:299–338.
45. Ohl, C.-D., and B. Wolfrum. 2003. Detachment and sonoporation of adherent HeLa cells by shock wave-induced cavitation. *Biochim. Biophys. Acta.* 1624:131–138.
46. Hutson, M. S., Y. Tokutake, M. S. Chang, J. W. Bloor, S. Venakides, D. P. Kiehart, and G. S. Edwards. 2003. Forces for morphogenesis investigated with laser microsurgery and quantitative modeling. *Science.* 300:145–149.
47. Khodjakov, A., R. W. Cole, B. R. Oakley, and C. L. Rieder. 2000. Chromosome-independent mitotic spindle formation in vertebrates. *Curr. Biol.* 10:59–67.
48. Khodjakov, A., C. L. Rieder, G. Sluder, G. Cassels, O. Sibon, and C. L. Wang. 2002. De novo formation of centrosomes in vertebrate cells arrested during *S* phase. *J. Cell Biol.* 158:1171–1181.